

PAPER

The effect of pre-plasma formation under nonlocal transport conditions for ultra-relativistic laser-plasma interaction

To cite this article: M Holec *et al* 2018 *Plasma Phys. Control. Fusion* **60** 044019

View the [article online](#) for updates and enhancements.

You may also like

- [Identifying the source of super-high energetic electrons in the presence of pre-plasma in laser-matter interaction at relativistic intensities](#)
D. Wu, S.I. Krasheninnikov, S.X. Luan et al.
- [Improvement in the heating efficiency of fast ignition inertial confinement fusion through suppression of the preformed plasma](#)
Y. Arikawa, S. Kojima, A. Morace et al.
- [Efficient laser acceleration of deuteron ions through optimization of pre-plasma formation for neutron source development](#)
Atsushi Sunahara, Takashi Asahina, Hideo Nagatomo et al.



IOP | ebooks™

Bringing together innovative digital publishing with leading authors from the global scientific community.

Start exploring the collection—download the first chapter of every title for free.

The effect of pre-plasma formation under nonlocal transport conditions for ultra-relativistic laser-plasma interaction

M Holec¹ , J Niki^{2,3} , M Vranic^{2,4}  and S Weber² 

¹ Centre Lasers Intenses et Applications, Université de Bordeaux-CNRS-CEA, UMR 5107, F-33405 Talence, France

² ELI-Beamlines, Institute of Physics, Academy of Sciences of the Czech Republic, 18221 Prague, Czechia

³ Faculty of Nuclear Sciences and Physical Engineering, Czech Technical University, 11519 Prague, Czechia

⁴ GoLP/Instituto de Plasmas e Fusão Nuclear, Instituto Superior Técnico, Universidade de Lisboa, 1049-001 Lisbon, Portugal

E-mail: milan.holec@u-bordeaux.fr

Received 4 December 2017, revised 5 February 2018

Accepted for publication 19 February 2018

Published 8 March 2018



Abstract

Interaction of high-power lasers with solid targets is in general strongly affected by the limited contrast available. The laser pre-pulse ionizes the target and produces a pre-plasma which can strongly modify the interaction of the main part of the laser pulse with the target. This is of particular importance for future experiments which will use laser intensities above $10^{21} \text{ W cm}^{-2}$ and which are subject to the limited contrast. As a consequence the main part of the laser pulse will be modified while traversing the pre-plasma, interacting with it partially. A further complication arises from the fact that the interaction of a high-power pre-pulse with solid targets very often takes place under nonlocal transport conditions, i.e. the characteristic mean-free-path of the particles and photons is larger than the characteristic scale-lengths of density and temperature. The classical diffusion treatment of radiation and heat transport in the hydrodynamic model is then insufficient for the description of the pre-pulse physics. These phenomena also strongly modify the formation of the pre-plasma which in turn affects the propagation of the main laser pulse. In this paper nonlocal radiation-hydrodynamic simulations are carried out and serve as input for subsequent kinetic simulations of ultra-high intensity laser pulses interacting with the plasma in the ultra-relativistic regime. It is shown that the results of the kinetic simulations differ considerably whether a diffusive or nonlocal transport is used for the radiation-hydrodynamic simulations.

Keywords: laser-plasma interaction, high-field, nonlocal transport

(Some figures may appear in colour only in the online journal)

1. Introduction

The interaction of high-power lasers with solid targets very often takes place under so-called nonlocal transport conditions. This means that the characteristic mean-free-path (mfp) of the transported physical quantities, e.g. electrons or photons, is of the order, or larger, than the characteristic gradient scale length of the thermodynamic variables, such as density and/or temperature. Under these conditions thermal and

radiative transport can no longer be described by the usual diffusive approach on which classic hydrodynamic plasma models are based. Non-locality is in general characterized by the quantity $\text{Kn} = \lambda/L$, where λ is the mfp of particles and L the plasma inhomogeneity scale length. The dimensionless quantity Kn is called the Knudsen number in standard fluid dynamics [1–5].

In the context of heat transport, it is appropriate to derive the characteristic scale length from the profile of the plasma

electron temperature T_e (using its gradient ∇T_e) and define $L = T_e/|\nabla T_e|$. It can also be expressed as $L = 1/k$, where k is the dominant component of the temperature profile in Fourier k -space. A characteristic scale length could also be based on the profile of the electron density n_e . However, classical hydrodynamic codes rely only on the heat diffusion approximation giving the local heat flux $\mathbf{q} = -\kappa_e \nabla T_e$. In order to quantify non-locality of the transport we use as Knudsen number for the electron thermal transport the expression $\text{Kn}^e = \lambda^e |\nabla T_e|/T_e$, where λ^e is the electron mfp. Similarly, the photon Knudsen number is defined as $\text{Kn}^p = \lambda^p |\nabla T_e|/T_e$, where λ^p is the photon mfp. The diffusion approximation is valid only for $\text{Kn} \ll 1$ (in particular, the theory gives $\text{Kn}^e \ll 0.06/\sqrt{Z}$ for Z the average ion charge [5]). Although, this is not usually the case for laser plasma as shown in the simulations in section 4.

In general the transport conditions in the laser-heated plasma cover the whole range of transport regimes from very diffusive to ballistic. The interaction of high power lasers with a solid target leads to creation of a shock wave driven by the exerted ablative pressure. The matter in the shock plateau is cold and compressed. The transport under these conditions is diffusive for both, electrons and photons, i.e. opaque and collisional. The Chapman–Enskog expansion method is a valid approach under these conditions [6]. The opposite regime is the strongly underdense plasma far out in the corona where the transport of electrons is basically free-streaming and radiation is no longer absorbed. These two regimes can be accommodated in straightforward ways from the physics and numerics point of view. The difficult part is the regime in between these two extremes. In particular, the energy of the laser beam deposited in the vicinity of the critical plane is further transported, partially into the target, thus leading to a creation of the *conduction zone* spanning from just outside the ablation front to the critical plane. The nature of the transport is getting more nonlocal for both electrons and photons with increasing temperature of the corona. Thermal transport and radiative transport are strongly interdependent and depend on the atomic number of the ablated material. It is this regime which is of prime importance as it determines the location of the critical plane and ablative pressure driving the main shock wave [3, 4]. The plasma profile and the temperature are strongly affected by these nonlocal processes [7], which may also lead to a significant effect on the high-power laser interaction as demonstrated in this work. A correct treatment of the ablation process requires an accurate non-local radiation-hydrodynamics, which has been demonstrated in [8–12] during last several decades.

Ablation physics under nonlocal transport conditions is of importance for two main applications:

- pre-pulse physics in (ultra-)high intensity laser-solid interaction due to the limited contrast available for high-power lasers [13, 14],
- shock wave creation in inertial confinement fusion under direct-drive or shock-ignition conditions [15–17].

In both cases the laser-plasma interaction conditions may take place under strong nonlocal transport conditions.

In this paper, we present details of the ablative plasma creation due to the high-power laser pre-pulse. This is of particular interest to forthcoming high-power laser installation such as ELI-Beamlines [18–20], APOLLON [21], SULF [22] and others [23].

Section 2 briefly describes the importance of nonlocal transport in the context of high-power laser physics. A new nonlocal transport hydrodynamic model (NTH) focused on laser-heated plasma simulations is presented in section 3 in order to address related kinetic effects. Section 4 shows actual radiation-hydrodynamic simulations and shows the nonlocal transport effect on high-power laser pre-pulse physics, which is further extended in section 5, where the results of particle-in-cell (PIC) simulation are presented demonstrating the main pulse interaction with the generated pre-plasma.

2. The importance of nonlocal hydrodynamics in high-power laser physics

The advent of laser technologies opens new opportunities in the extreme high-field physics or the fast ignition concept for inertial confinement fusion investigation. In this paper, we focus on the most powerful laser (10 PW) under construction at the ELI Beamlines laser facility, which is called L4 [19]. It is based on the solid-state Nd:glass laser technology using the chirped pulse amplification (CPA) [24], where the stretched and subsequently amplified pulse undergoes a final step of compression in time. The use of mixed Nd:glass CPA laser providing spectral bandwidth allows effective pulse compression [25], and thus, the peak power of 10 PW. The principal laser pulse can reach the energy of 1.5 kJ, which should be compressed into an interval of less than 150 fs.

The extreme power of the L4 beamline is better expressed in terms of laser intensity, which actually addresses the laser-matter interaction phenomena. The proposed experiments to be realized on the L4 beamline go well above the relativistic laser intensity limit possibly reaching intensities of $10^{24} \text{ W cm}^{-2}$, which goes far beyond the hydrodynamic limit ($\approx 10^{15} \text{ W cm}^{-2}$). However, the high intensity laser pulse is unavoidably accompanied by a pre-pulse, which, in the case of 10 PW, must be taken into account with a special care in experimental settings. According to [19], the L4 beamline will generate a 10 ns laser pedestal, which should be kept, in the optimal laser adjustment, within the range of contrast about 10^{11} with respect to the high intensity pulse. However, the laser contrast of 10^{10} can probably be expected. Consequently, the worst scenario includes a pre-pulse intensity $10^{13} \text{ W cm}^{-2}$, which, in combination with a several ns long duration, provides a significant irradiation by the laser leading to the formation of a non-negligible pre-plasma. The quantification of spatial scale of such a pre-plasma is a crucial information necessary for the proper main pulse interaction.

Modeling of the pre-plasma formation is very challenging and since the time and spatial scales are macroscopic, where Lagrangian hydrodynamics represents the most convenient simulation tool. However, the standard hydrodynamic model given by Euler or Navier–Stokes equations cannot address many physical phenomena emerging from the non-local nature of energy transport, which is typical for laser-heated plasma experiments. In general, one of the most important goals of the ablative physics (the expansion of plasma fluid) is to describe properly the kinetics of plasma under the condition of high temperatures and relatively low densities during the irradiation by laser. Such conditions are best described by the Knudsen number defined earlier (see section 1), where the plasma ablation pre-dominantly falls into the nonlocal regime of transport.

3. NTH model of laser-heated plasma

The NTH model of laser-heated plasma, which was introduced in detail in [26, 27], treats the plasma as a two temperature single-fluid including deposition of the laser energy and the nonlocal transport of radiation and electron heat. The hydrodynamic quantities, the mass density ρ , momentum density $\rho \mathbf{u}$ and total energy density $E = \frac{1}{2} \rho \mathbf{u} \cdot \mathbf{u} + \rho \varepsilon_i + \rho \varepsilon_e$ with \mathbf{u} being the plasma fluid velocity and $\varepsilon_e, \varepsilon_i$ the specific internal electron and ion energy density respectively, are described by the Euler equations in the Lagrangian frame

$$\frac{d\rho}{dt} = -\rho \nabla \cdot \mathbf{u}, \quad (1)$$

$$\rho \frac{d\mathbf{u}}{dt} = -\nabla(p_i + p_e), \quad (2)$$

$$\rho \left(\frac{\partial \varepsilon_i}{\partial T_i} \frac{dT_i}{dt} + \frac{\partial \varepsilon_i}{\partial \rho} \frac{d\rho}{dt} \right) = -p_i \nabla \cdot \mathbf{u} - G(T_i - T_e), \quad (3)$$

$$\rho \left(\frac{\partial \varepsilon_e}{\partial T_e} \frac{dT_e}{dt} + \frac{\partial \varepsilon_e}{\partial \rho} \frac{d\rho}{dt} \right) = -p_e \nabla \cdot \mathbf{u} + G(T_i - T_e) - \nabla \cdot (\mathbf{q}_e + \mathbf{q}_R + \mathbf{q}_L), \quad (4)$$

where T_i is the temperature of ions, T_e the temperature of electrons, p_i the ion pressure, p_e the electron pressure, \mathbf{q}_e the flux of energy due to electrons, \mathbf{q}_R the flux of energy due to radiation, \mathbf{q}_L the laser energy flux (the Poynting vector). The rate of heat exchange between electrons and ions is given by $G = \rho \nu_e \partial \varepsilon_e / \partial T_e$, where ν_e is the electron collision frequency. The equation of state based on the SESAME tables [28, 29] provides the terms $p_e, p_i, \frac{\partial \varepsilon_e}{\partial T_e}, \frac{\partial \varepsilon_i}{\partial T_i}, \frac{\partial \varepsilon_e}{\partial \rho}, \frac{\partial \varepsilon_i}{\partial \rho}$ thermodynamically closing the equations (1)–(4). The energy fluxes of electrons and radiation are obtained from the nonlocal transport closure in the form

$$\mathbf{q}_e + \mathbf{q}_R = \int_{4\pi} \mathbf{n} (I^e + I^p) d\mathbf{n}, \quad (5)$$

where $I^e = \int f^e |\mathbf{v}| \frac{m_e |\mathbf{v}|^2}{2} |\mathbf{v}|^2 d|\mathbf{v}|$ and $I^p = \int f^p \frac{h^4 \nu^3}{c^2} d\nu$ are electron intensity (the energy flux of the electron distribution f^e

integrated over velocity magnitude $|\mathbf{v}|$) and radiation intensity (the energy flux integrated photon distribution function f^p , where ν is photon frequency and h the Planck constant), respectively. These represent the transport of energy in plasmas and are modeled by the Bhatnagar–Gross–Krook (BGK [30]) type of nonlocal electron transport model [26, 27]

$$\mathbf{n} \cdot \nabla I^e = \left(\frac{n_e k_B}{8 \lambda^e \pi^{\frac{3}{2}}} \sqrt{\frac{2 k_B T_e}{m_e}} \right) T_e - \frac{I^e}{8 \lambda^e}, \quad (6)$$

where k_B the Boltzmann constant, n_e and n_i the electron and ion density respectively, and λ^e the electron mean free path of thermal electrons due to electron–ion and electron–electron collisions defined by Spitzer and Härm (SH) [31]. Similarly the radiation transport equation [2] is given as

$$\mathbf{n} \cdot \nabla I^p = \frac{a T_e^4 - I^p}{\lambda^p}, \quad (7)$$

where λ^p is the photon mean free path based on the mean Planck opacity presented in [32], which are valid for temperatures from 10 to 500 eV and electronic densities from 10^{18} to 10^{23} cm^{-3} .

It is worth mentioning, that the above transport equations can be distinguished from the previous nonlocal electron transport and radiation transport models traditionally used in radiation-hydrodynamics codes, since it does not use the diffusion approximation (the lowest anisotropy of transport), while the diffusion asymptotic is still full-filled [26, 33]. The importance of the nonlocal electron transport has been recently observed experimentally, where it was demonstrated that the classical diffusive hydrodynamics fails to model the real behavior of the plasma. In contrast, the NTH model succeeds to predict a complex plasma behavior [12].

The employed model of laser propagation and absorption [34], which provides the energy flux (the Poynting vector) \mathbf{q}_L is based on the solution of Helmholtz equation for the electric field \mathbf{E}_L in 1D

$$\frac{\partial^2 E_L}{\partial z^2} = -\frac{\omega^2}{c^2} \varepsilon E_L, \quad (8)$$

where ω is the angular laser frequency, c speed of light in vacuum, E_L the transverse component of the electric field, not distinguishing the linear polarizations for normal incidence of the laser. The relative complex permittivity ε is given by [35]

$$\varepsilon = 1 - \frac{\omega_{pe}^2}{\omega(\omega + i\nu_e)}, \quad (9)$$

where ω_{pe} represents the electron plasma frequency and ν_e the electron collision frequency, which has fundamental importance for the quantitative evaluation of inverse-bremsstrahlung laser absorption mechanism [36].

4. Radiation hydrodynamic simulations

4.1. Simulation parameters

The hydrodynamic simulations were performed using our state-of-art plasma Euler and transport equation hydrodynamic code

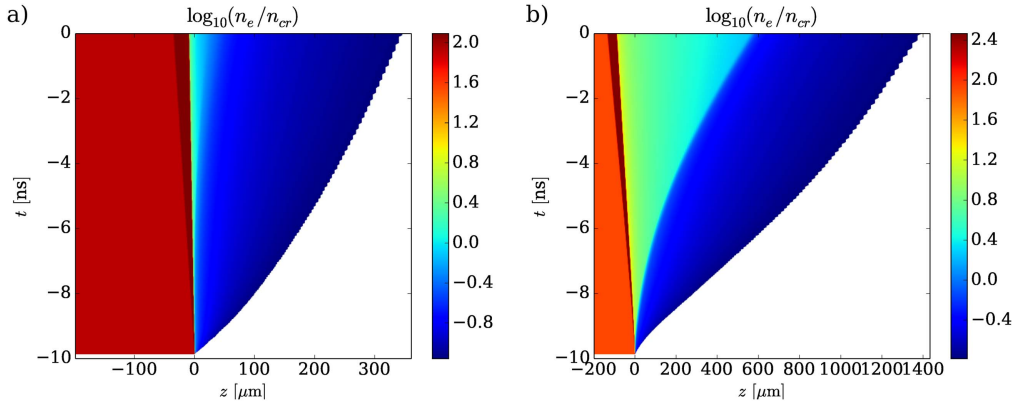


Figure 1. The pre-plasma formation during 10 ns of the pre-pulse is shown. The time evolution of the electron density profile for intensities $10^{11} \text{ W cm}^{-2}$ (main pulse intensity $10^{22} \text{ W cm}^{-2}$) (a) and $10^{13} \text{ W cm}^{-2}$ (main pulse intensity $10^{24} \text{ W cm}^{-2}$) (b) can be seen in (a) and (b), respectively (the low density part $n_e < 0.1n_c$ is omitted). Detailed profiles corresponding to time 0 can be found in figure 2. The formation of the conduction zone can be easily identified by the turquoise color regions.

(PETE). PETE is based on the 1D formulation of the NTH model presented in section 3, where the Euler equations are numerically solved by the compatible hydrodynamic scheme on a staggered computational mesh [37] and the nonlocal transport equations for electrons and radiation are obtained from the high-order finite element DG-BGK&Ts scheme proposed recently [33]. All of the transported particles are treated as one energy group, known as the gray-body approximation in the context of radiation transport.

In principle, the effects of laser pre-pulse lead to several scenarios due to the early laser pedestal. The pre-plasma creation at the front side of the target is always observed once the pre-pulse intensity exceeds the limit of plasma creation (approximately 10^9 W cm^{-2} for ns-prepulses). Depending on the pre-pulse intensity, the pre-plasma expansion velocity can be estimated. In the case of a sufficiently high pre-pulse intensity the interaction launches a shock which propagates into the target [13, 14, 38–40]. The higher the pre-pulse intensity, the faster the pre-plasma expansion and also the higher the shock velocity. All of the latter effects lead to a specific pre-plasma profile and its variation can alter the final outcome of the high intensity pulse interaction with matter (pre-plasma).

We used a thick foil target ($200 \mu\text{m}$) made of CH plastic with $Z = 3.5$ and the electron density in solid state $n_e \simeq 86 n_{cr}$. The Lagrangian computational mesh consisted of 450 cells, where the first $3 \mu\text{m}$ were covered by 250 cells with geometric factor 0.975 (laser absorption takes place at a very fine mesh), and the remaining part of the target was spatially discretized by 200 cells with geometric factor 0.981. This way we obtained an excellent discretization of the part of the target from which the pre-plasma is formed, and also captured the shock propagation in direction inward the target.

4.2. NTH simulations of the L4 pre-pulse

In order to analyze the actual effect of pre-pulse of the L4 beamline, we performed a set of simulations taking into account three different intensities, considering the Nd:glass

laser pulse of wave length $\lambda_{L4} = 1.057 \mu\text{m}$ with corresponding non-relativistic critical electron density $n_{cr} \approx 1.01 \times 10^{21} \text{ cm}^{-3}$. Since the 10 PW can provide peak intensities 10^{22} , 10^{23} , and $10^{24} \text{ W cm}^{-2}$ (with respect to the focal spot), pre-pulse intensities of 10^{11} , 10^{12} , and $10^{13} \text{ W cm}^{-2}$ of 10 ns duration can be expected (considering an excellent contrast 10^{11} [19]). However, also the lower contrast 10^{10} was used later on in the kinetic simulations of the main pulse to show its dramatic effect on the interaction as described in section 5.

In order to address the dominant physical phenomena, we distinguish between four different regions [26, 41], since they are naturally created during the laser plasma interaction as can be seen in figure 1, and in more detail in figure 2. It can be observed, that the shock wave propagates in negative direction with approximately constant velocity, while the thickness of the conduction zone grows in the opposite direction and faster than linear in time. A closer look at figure 2(b) provides a natural characterization of different plasma conditions, namely four different zones. When describing the plasma profile from right to left, i.e. in the direction of propagation of the laser, the lowest density plasma corona is labeled ‘III’ and corresponds to the non-zero energy flux of laser (dashed magenta line), the next zone labeled ‘II’ is called *the conduction zone* due to its origin based on the nonlocal transport effects (the dominant energy flux is due to radiation) and exhibits low density continuously increasing until the high density of the compressed target, another characteristic zone, labeled ‘I’. The boundary between ‘II’ and ‘I’ is the so-called ablation front and can be easily distinguished by the hydrodynamic flux $p\mathbf{v}$ orientation (wherever $p\mathbf{v} > 0$, plasma ablates), where p is the plasma pressure and \mathbf{v} the plasma fluid velocity. Certainly, the hydrodynamic flux dominates in zone ‘II’ since the electron transport is suppressed by collisions. The remaining part of the yet unchanged target is labeled ‘0’.

The conduction zone size is one of the important parameters, which affect the propagation of the main pulse

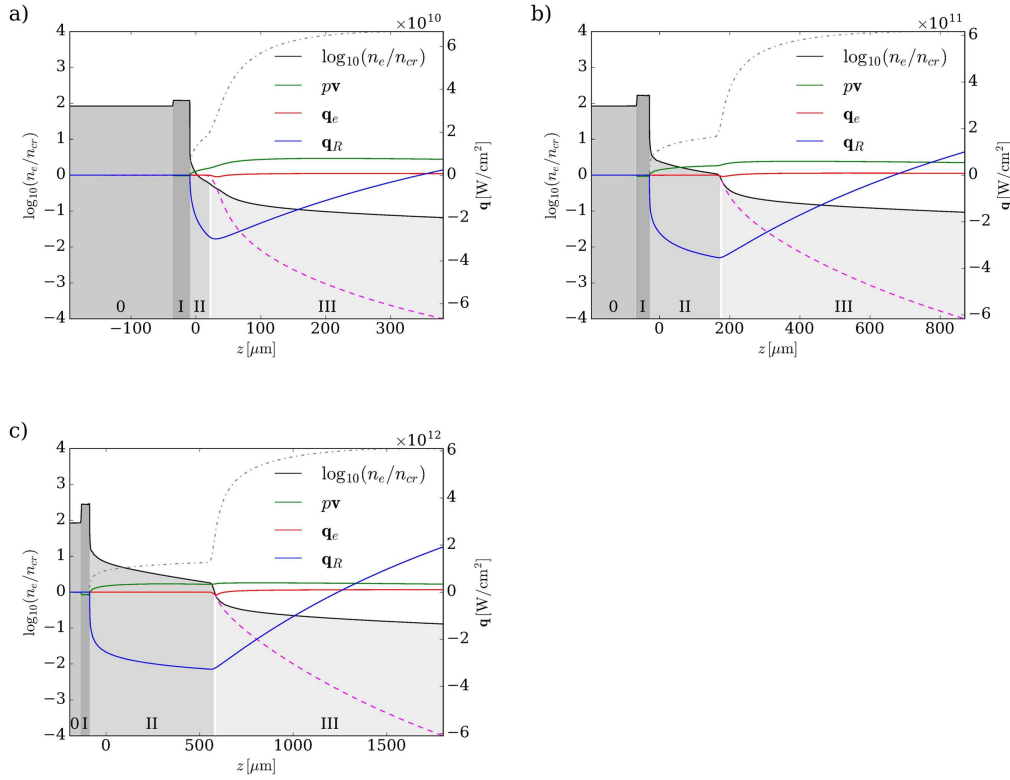


Figure 2. The plasma profile after 10 ns of a constant laser pre-pulse irradiation of intensity (a) $10^{11} \text{ W cm}^{-2}$ (main pulse intensity $10^{22} \text{ W cm}^{-2}$), (b) $10^{12} \text{ W cm}^{-2}$ (main pulse intensity $10^{23} \text{ W cm}^{-2}$), and (c) $10^{13} \text{ W cm}^{-2}$ (main pulse intensity $10^{24} \text{ W cm}^{-2}$), where different zones: 0 cold target; I shocked target; II conduction zone; and III plasma corona; are shown. The profiles of energy fluxes contributing to the energy equation (4) emphasize the dominance of each of the transport phenomena, i.e. fluid, electron, and radiation transport of energy, in each of the zones. Additionally, the dashed magenta line plots the profile of laser flux q_L , and the dashed-dot gray line the profile of electron temperature T_e with its maximum: (a) 59 eV; (b) 152 eV; and (c) 383 eV.

arriving at the end of the pre-pulse, as is shown in section 5. In what follows, we describe in detail each of the simulation with respect to the pre-pulse intensity. Extension of the pre-plasma, and, in particular, the thickness of the conduction zone characterizes best the effect of the actual high intensity laser pulse interaction with solid targets.

Due to the effect of nonlocal energy transport on the pre-plasma formation (defined as plasma with density more than 10% of the critical density in the following text), it is observed, that in spite of the excellent laser contrast, the existing pre-pulse unavoidably forms a pre-plasma. Depending on the pre-pulse intensity, the pre-plasma reaches 380, 900, and $1800 \mu\text{m}$, where the conduction zone extends over 25, 200, and $700 \mu\text{m}$, as can be seen in figure 2. The inward motion of the launched shock, which propagates inside the target, exhibits an almost constant velocity approximately 3.3 , 6.5 , and 11 km s^{-1} , as function of the increasing laser intensity.

The nonlocal hydrodynamic model presented in section 3 and implemented into our code PETE covers all relevant aspects of physics and thereby provides a valuable tool for predictive simulations of future experiments. In spite of some limitations of our hydrodynamic simulations (1D channeling effect for example), the nature of coupled nonlocal radiation and electron transport has been observed for the first time in hydrodynamic

simulations, where the BGK model provides a first-principles based approach and is valid under any transport regime. Nevertheless, the proper physics of nonlocal transport should be further investigated by using a multi-energy-group extension for both, radiation and electrons, while PETE currently uses an one-group model.

4.3. Comparison of NTH and classical hydrodynamics

In the previous section, we could see that the nonlocal transport of energy due to radiation and electrons fluxes is responsible for the conduction zone formation (region II in figure 2). In order to stress the importance of the nonlocal transport model, we performed a simulation of exactly the same parameters, where the classical hydrodynamics was used, which includes the effect of transport by the means of the electron diffusion only, i.e. the classical heat conduction by SH [31].

In figure 3, we show the resulting difference in the density profile (logarithmic scale). In principle, both profiles are in a good agreement except for the pre-plasma part referred as conduction zone (see figure 2(b)). The strong nonlocal radiation fluxes lead to substantial increase of the density by transporting energy from the critical plane to the head of the ablation front. These structures are typically called *double ablation front* as investigated mainly in the context of inertial

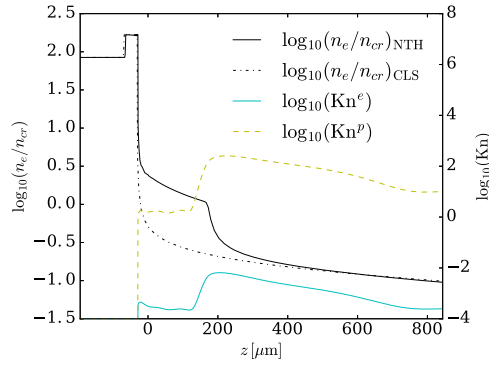


Figure 3. The electron density profile formed due to the 10 ns pre-pulse of intensity $10^{12} \text{ W cm}^{-2}$ (corresponding to the peak intensity $10^{23} \text{ W cm}^{-2}$) is shown. The solid line correspond to the simulation using nonlocal transport hydrodynamic model referred to as NTH, in comparison, the dashed line represent simulation result of the classical hydrodynamics referred to as CLS including the SH diffusion transport model. Also, detailed profiles of electron and photon Knudsen numbers along the plasma profile are shown in the case of NTH.

fusion [34, 42, 43]. The effect of change in the density profile (ramp), however, leads to a significantly different interaction between the arriving high-intensity main pulse and the target.

In the diffusion simulation, 5% of the free streaming flux was applied via the flux limiter [44], in order to obtain a similar plasma expansion scale as in the case of the nonlocal transport simulations.

5. Particle in cell simulations

To illustrate the effect of the pre-plasma on the propagation of the main pulse towards the solid target, we performed a series of simulations with OSIRIS [45], a massively parallel PIC code [46] with a radiation reaction module [47]. The initial plasma density distributions with and without nonlocal transport are mapped from the hydro simulation results displayed in figure 3. We assumed that the plasma will be fully ionized by the main laser. For sections of the plasma profiles from figure 3 that were not fully ionized by the pre-pulse, we used a multiplication factor that accounts for the increase in electron density due to the subsequent ionization.

The pulse duration is 150 fs (FWHM). The laser transverse profile is taken to be a plane wave, and the electric field of the laser is perpendicular to the simulation plane. The simulation box is $636 \mu\text{m}$ long and $10 \mu\text{m}$ wide, with periodic transverse boundary conditions. We simulate the range of space from figure 3 between $z = -159 \mu\text{m}$ and $z = 477 \mu\text{m}$. The numerical resolution is $40\,000 \times 600$ cells with a time step $dt = 0.021 \text{ fs}$. Three particle species were used: electrons, carbon ions and hydrogen ions (protons), with 9 macro-particles per cell for each species. The laser is initialized from the right-hand side wall of the simulation box, and the time in this section is counted from the beginning of the PIC

simulation (e.g. at $t = 150 \text{ fs}$ from the beginning of the simulation, the peak of the laser was being initialized at $z = 477 \mu\text{m}$).

The laser absorption with and without nonlocal transport is shown in figure 4. Panel (a) corresponds to the case with a lower main laser intensity $10^{22} \text{ W cm}^{-2}$ and a contrast of 10^{10} , while panel (b) corresponds to a higher main laser intensity $10^{23} \text{ W cm}^{-2}$ and an optimal high contrast of 10^{11} . Each absorption curve has two parts: a slow absorption due to interacting with the pre-plasma in the conduction zone ($t < 1.8 \text{ ps}$), and a fast absorption by the main target once the pulse reaches the ablation front.

The main differences between the cases with and without the nonlocal transport model used in the simulations of the prepulse can be noticed in the former conduction zone. Even though the conduction zone is not relativistically critical, it is dense enough to interact nonlinearly with the laser. This is confirmed in figure 5 that shows the electron density and the electromagnetic energy density at $t = 1.79 \text{ ps}$. The laser strongly filaments as shown in figure 5(c). By this time, the laser energy has been partially absorbed in the conduction zone for both cases: 18.5% of energy has been absorbed for the diffusive case and 54.8% for the case with nonlocal transport. This is not surprising, as the plasma density is several times higher in the conduction zone than in the case without nonlocal transport. Therefore, the pre-plasma reduces the interacting energy of the main laser already in the conduction zone, which diminishes the energy content delivered to the solid target. This effect is stronger in the case when the nonlocal transport is taken into account. Finally, a fraction of 11.8% laser energy gets reflected from the ablation front in the diffusive case, while this amounts to 3.1% for the nonlocal case. Figure 4(b) corresponds to a more intense laser ($I = 10^{23} \text{ W cm}^{-2}$) with a high contrast (10^{11}). In this case, 13.7% has been absorbed in the conduction zone for the diffusive case, and 61.1% for the nonlocal. The radiation reaction is taken into account for this simulation as high-frequency radiation emission becomes a significant depletion channel. This is more important for the case with nonlocal transport, because the conduction zone has higher electron density. Without radiation reaction taken into account, the conduction zone absorbs nearly a three times smaller fraction of the laser energy.

We are aware that the effects with longer characteristic wavelengths might not be captured due to a small transverse box size ($10 \mu\text{m}$, which corresponds to the laser focal spot diameter). This was a necessary compromise in order to simulate $>0.5 \text{ mm}$ long box containing areas of over-critical plasma density for several picoseconds. Nevertheless, the results indicate that nonlocality evidently affects the main pulse interaction with the pre-plasma as can be verified in figures 4 and 5.

To the best of our knowledge, this is the first time a very detailed description of the pre-plasma formation was included in the PIC simulation of a high-power laser interaction with a solid plastic target.

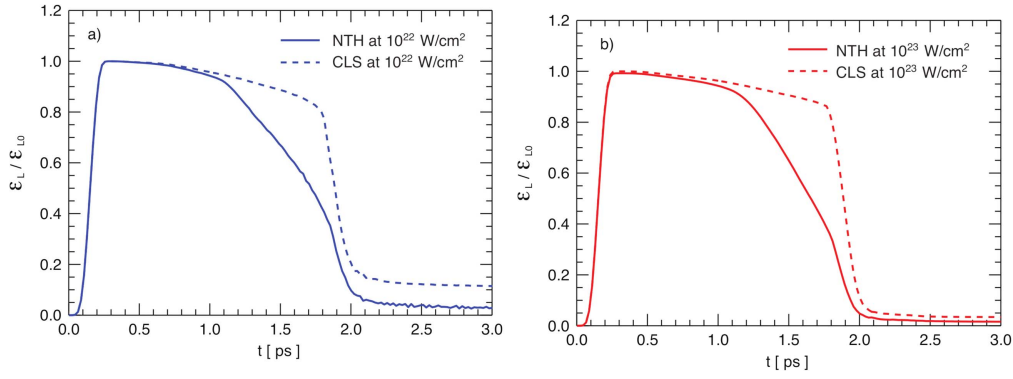


Figure 4. Laser energy as a function of time for the main laser intensity of (a) $10^{22} \text{ W cm}^{-2}$ (b) $10^{23} \text{ W cm}^{-2}$. The energy ϵ_L is normalized to the initial laser energy ϵ_{L0} . The initial plasma profiles are given in figure 2(b).

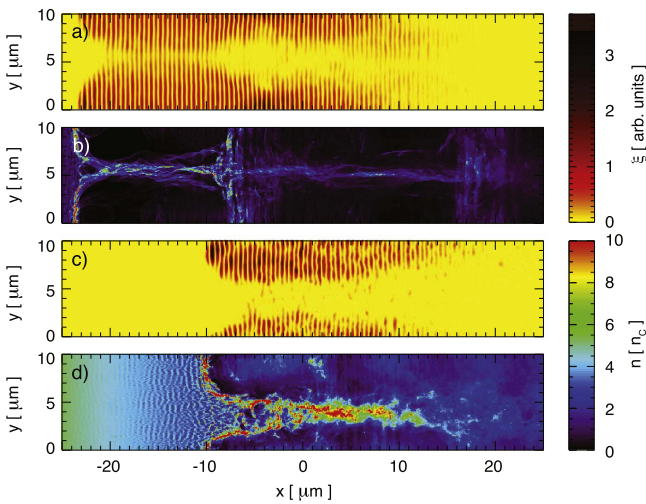


Figure 5. Interaction of the main laser pulse with plasma in the conduction zone. (a), (c) Electromagnetic energy density ξ and (b), (d) electron plasma density for $t = 1.79 \text{ ps}$. Panels (a), (b) correspond to the diffusive case; panels (c), (d) correspond to the case with nonlocal transport. The laser initial intensity is $10^{22} \text{ W cm}^{-2}$.

6. Conclusions

Nonlocal hydrodynamic simulations were performed in order to obtain theoretical insight into the pre-plasma formation for the next generation high-power lasers. The formation of conduction zone and overall pre-plasma expansion were studied in detail for different laser intensities. The evident effect of the nonlocal transport was addressed in the case of comparison with standard diffusion simulations. Based on the PIC simulations, we revealed the importance of detailed knowledge about the pre-plasma formation. In particular, the effect of nonlocal transport was justified, since the non-linear interaction of high-intensity laser with the pre-plasma formed in the simulations with the nonlocal transport model leads to a significant filamentation and overall absorption of the main pulse energy before reaching the target.

Acknowledgments

This work has been supported by the project High Field Initiative (HiFI) (CZ.02.1.01/0.0/0.0/15_003/0000449) and ELI Tools for Advanced Simulation (ELITAS) (CZ.02.1.01/0.0/0.0/16_013/0001793), both from European Regional Development Fund and Czech Technical University grant SGS16/247/OHK4/3T/14. This project has received funding from the EUROfusion project CfP-AWP17-IFE-CEA-01.

ORCID iDs

M Holec <https://orcid.org/0000-0001-7016-0729>
 J Nikl <https://orcid.org/0000-0003-0131-0628>
 M Vranic <https://orcid.org/0000-0003-3764-0645>
 S Weber <https://orcid.org/0000-0003-3154-9306>

References

- [1] Mihalas D and Mihalas B 1985 *Foundations of Radiation Hydrodynamics* (New York: Oxford University Press)
- [2] Castor J 2004 *Radiation Hydrodynamics* (Cambridge: Cambridge University Press)
- [3] Zeldovich Y B and Raizer Y P 2002 *Physics of Shock Waves and High-Temperature Hydrodynamic Phenomena* (New York: Dover)
- [4] Atzeni S and Meyer-Ter-Vehn J 2004 *The Physics of Inertial Fusion* (Oxford: Clarendon)
- [5] Brantov A V and Bychenkov V Y 2013 *Plasma Phys. Rep.* **39** 698
- [6] Chapman S and Cowling T G 1952 *Mathematical Theory of Nonuniform Gases* (Cambridge: Cambridge University Press)
- [7] Nicolai P, Feugeas J L, Nguyen-Bui T, Tikhonchuk V, Antonelli L, Batani D and Maheut Y 2015 *Phys. Plasmas* **22** 042705
- [8] Luciani J F, Mora P and Virmont J 1983 *Phys. Rev. Lett.* **51** 1664–7
- [9] Schurtz G, Nicolai P and Busquet M 2000 *Phys. Plasmas* **7** 4238–49
- [10] Manheimer W, Colombant D and Goncharov V 2008 *Phys. Plasmas* **15** 083103

- [11] Sorbo D D, Feugeas J L, Nicolai P, Olazabal-Loume M, Dubroca B, Guisset S, Touati M and Tikhonchuk V 2015 *Phys. Plasmas* **22** 082706
- [12] Falk K, Holec M, Fontes C J, Fryer C L, Greeff C W, Johns H M, Montgomery D S, Schmidt D W and Smid M 2018 *Phys. Rev. Lett.* **120** 025002
- [13] Esirkepov T et al 2014 *Nucl. Instrum. Methods* **745** 150
- [14] Utsumi T, Matsukado K, Daido H, Esirkepov T and Bulanov S 2004 *Appl. Phys. A* **79** 1185
- [15] Betti R and Hurricane O 2016 *Nat. Phys.* **12** 435
- [16] Batani D et al 2014 *Nucl. Fusion* **54** 054009
- [17] Batani D et al 2014 *Phys. Plasmas* **21** 032710
- [18] The Extreme Light Infrastructure project: ELI <http://eli-beams.eu>
- [19] Rus B et al 2015 *Proc. SPIE* **9515** 951501
- [20] Weber S et al 2017 *Matter Radiat. Extremes* **2** 149
- [21] Zou J et al 2015 *High Power Laser Sci. Eng.* **3** e2
- [22] Gan Z et al 2017 *Opt. Express* **25** 5169
- [23] Danson C, Hillier D, Hopps N and Neely D 2015 *High Power Laser Sci. Eng.* **3** e3
- [24] Treacy E 1969 *IEEE J. Quantum Electron.* **QE-5** 454
- [25] Strickland D and Mourou G 1985 *Opt. Commun.* **56** 219
- [26] Holec M, Nikl J and Weber S 2017 Nonlocal transport hydrodynamic model for laser heated plasmas *Phys. Plasmas* submitted
- [27] Holec M 2016 Numerical modeling of nonlocal energy transport in laser-heated plasmas *Doctoral Thesis* Czech Technical University (<http://hdl.handle.net/10467/68302>)
- [28] Group T 1983 SESAME report on the Los Alamos equation-of-state library *Technical Report* LALP-83-4 Los Alamos National Laboratory, Los Alamos
- [29] Lyon S P and Johnson J D 1992 SESAME: the Los Alamos National Laboratory equation of state database *Technical Report* LA-UR-92-3407 Los Alamos National Laboratory, Los Alamos
- [30] Bhatnagar P, Gross E and Krook M 1954 *Phys. Rev.* **94** 511–25
- [31] Spitzer J L and Härm R 1953 *Phys. Rev.* **89** 977
- [32] Rubiano J, Rodriguez R, Gil J, Florido R, Martel P, Mendoza M, Suarez D and Minguez E 2008 *J. Phys.: Conf. Ser.* **112** 042006
- [33] Holec M, Limpouch J, Liska R and Weber S 2017 *Int. J. Numer. Methods Fluids* **83** 779
- [34] Nikl J, Holec M, Zeman M, Kuchařík M, Limpouch J and Weber S 2017 Macroscopic laser-plasma interaction under strong non-local transport conditions for coupled matter and radiation *Matter Radiat. Extremes* submitted
- [35] Born M and Wolf E 1999 *Principles of Optics: Electromagnetic Theory of Propagation, Interference and Diffraction of Light* (Cambridge: Cambridge University Press)
- [36] Eidmann K, Meyer-ter-Vehn J, Schlegel T and Hüller S 2000 *Phys. Rev. E* **62** 1202
- [37] Shashkov M 1996 *Conservative Finite-Difference Methods on General Grids* (Boca Raton, FL: CRC Press)
- [38] Flacco A, Guemnie-Tafo A, Nuter R, Veltcheva M, Batani D, Lefebvre E and Malka V 2008 *J. Appl. Phys.* **104** 103304
- [39] Carroll D C et al 2009 *C. R. Phys.* **10** 188
- [40] McKenna P et al 2008 *Laser Part. Beams* **26** 591
- [41] Goncharov V N et al 2006 *Phys. Plasmas* **13** 012702
- [42] Sanz J, Betti R, Smalyuk V, Olazabal-Loumé M, Drean V, Tikhonchuk V, Ribeyre X and Feugeas J 2009 *Phys. Plasmas* **16** 082704
- [43] Drean V, Olazabal-Loumé M, Sanz J and Tikhonchuk V 2010 *Phys. Plasmas* **17** 122701
- [44] Rosen M D et al 1979 *Phys. Fluids* **22** 2020
- [45] Fonseca R A et al 2002 *OSIRIS: A Three-Dimensional, Fully Relativistic Particle in Cell Code for Modeling Plasma Based Accelerators* (Berlin: Springer)
- [46] Fonseca R A, Vieira J, Fiuza F, Davidson A, Tsung F, Mori W B and Silva L O 2013 *Plasma Phys. Control. Fusion* **55** 124011
- [47] Vranic M, Martins J L, Fonseca R A and Silva L O 2016 *Comput. Phys. Commun.* **204** 141